Accelerated design of architectured ceramics with tunable thermal resistance via a hybrid machine learning and finite element approach

E. Fatehi [a,b], H. Yazdani Sarvestani [b], B. Ashrafi [b,*], A.H. Akbarzadeh [a,c,*]

[a] Department of Bioresource Engineering, McGill University, Montreal, QC H3A0C3, Canada
[b] Aerospace Manufacturing Technology Center, National Research Council Canada, Montreal, QC H3T 2B2, Canada
[c] Department of Mechanical Engineering, McGill University, Montreal, QC H3A0C3, Canada

HIGHLIGHTS

- Exploring the effect of angle and number of tiles on the thermomechanical behavior of topologically interlocked ceramics.
- Developing a novel hybrid FEA and ML algorithm for exploring the performance of architectured ceramics with uniform and varied-angle designs.
- Finding new interlocked designs with enhanced thermo-mechanical performances using Neural Networks.
- Finding an optimum varied-angle architectural design that improves 30% energy dissipation and 80% strain energy reduction of brittle ceramics.

GRAPHICAL ABSTRACT
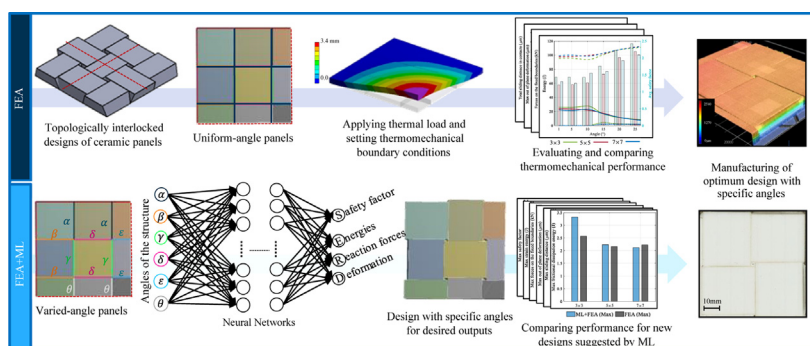
ABSTRACT

Topologically interlocked architectures can transform brittle ceramics into tougher materials, while making the material design procedure a cumbersome task since modeling the whole architectural design space is not efficient and, to a degree, is not viable. We propose an approach to design architectured ceramics using machine learning (ML), trained by finite element analysis data and together with a self-learning algorithm, to discover high-performance architectured ceramics in thermomechanical environments. First, topologically interlocked panels are parametrically generated. Then, a limited number of designed architectured ceramics subjected to a thermal load is studied. Finally, the multilinear perceptron is employed to train the ML model in order to predict the thermomechanical performance of architectured panels with varied interlocking angles and number of blocks. The developed feed-forward artificial neural network framework can boost the architectured ceramic design efficiency and open up new avenues for controllability of the functionality for various high-temperature applications. This study demonstrates that the architectured ceramic panels with the ML-assisted engineered patterns show improvement up to 30% in frictional energy dissipation and 7% in the sliding distance of the tiles and 80% reduction in the strain energy, leading to a higher safety factor and the structural failure delay compared to the plain ceramics.

© 2021 The Authors. Published by Elsevier Ltd. This is an open access article under the CC BY-NC-ND license (http://creativecommons.org/licenses/by-nc-nd/4.0/).

* Corresponding authors at: Department of Bioresource Engineering, McGill University, Montreal, QC H3A0C3, Canada (A.H. Akbarzadeh) and 2107 chemin Polytechnique, Montreal, QC H3T 1J4, Canada (B. Ashrafi).
E-mail addresses: Erfan.Fatehi@nrc-cnrc.gc.ca (E. Fatehi), hamidreza.yazdani@nrc-cnrc.gc.ca (H. Yazdani Sarvestani), behnam.ashrafi@nrc-cnrc.gc.ca (B. Ashrafi), hamid.akbarzadeh@mcgill.ca (A.H. Akbarzadeh).

1. Introduction

Ceramics are used in a wide range of industrial sectors, including electronics [1], aerospace [2], medicine and biomedical devices [3–5], owing to their excellent properties such as oxidation resistance, low electrical conductivity, high refractory and maintaining their mechanical properties at high temperatures [6]. The low thermal conductivity of ceramics is used to protect space shuttles and keep satellites safe from serious damages [2], while their thermal stability property is critical in hypersonic flights and propulsion applications [7]. In spite of the excellent thermomechanical properties of ceramics, they generally suffer from brittleness [6,8] that limits their multifunctional applications where ductility and toughness are required in addition to stiffness, strength and thermal resistance. Inspiration from natural and biological materials can assist to engineer the next generation of ceramics that can overcome the aforementioned drawback [9,10].

Superior mechanical properties of biological species, such as a combination of high strength and toughness, have inspired material scientists and engineers to develop advanced high-performance materials [11,12]. In biological composites (e.g. bones, shells, horns and teeth), brittle organic materials such as calcium carbonate, calcium phosphate (hydroxyapatite), and amorphous silica [13] are employed by nature to design biomaterials that offer a combination of high strength, stiffness, flexibility, fracture toughness, and wear resistance [14,15]. For example, the fracture toughness of abalone, conch shell and nacre with a brick and mortar microstructure [12,16], is up to seven times higher than their material constituent, i.e., calcium carbonate [17]. Tooth enamel, as the hardest material in vertebrates, has also shown high toughness due to its microstructure that consists of tightly packed hydroxyapatite rods [18]. As a universal construction principle, these biological materials are made of hard and stiff building blocks bonded by weaker interfaces [19]. This finely-tuned strategy can result in deformation/failure mechanisms that enable the amplification of toughness. For instance, the staggered architecture in nacre-like materials can result in progressive tablet sliding and crack blunting, deflecting, and bridging [20]. These microstructural designs have recently inspired the development of a new class of tough architectured structures out of brittle materials such as ceramic and glass [21,22].

One of the material design strategies to achieve superior mechanical performance is developing interlocked building blocks for architectured materials that acts as a strain hardening mechanism to localize damages and spread the deformation to a larger volume of brittle materials [19]. The resulting materials are called topologically interlocked materials (TIMs) [23,24]. Researchers have made considerable progress in the design and fabrication of TIMs to enhance their energy absorption and impact resistance capacity [25–28]. Toughness has been improved in brittle materials by interlocked and segmented designs [9,25]. The toughening mechanism is observed due to segmentation of blocks and the existence of weak interfaces (e.g. soft polymers such as ionomer or Ethylene-vinyl acetate (EVA) resins as an engineering replacement of protein in nacre) between microscale building blocks with tetrahedral, octahedral and cubic architectures [29–33]. These configurations offer a vast design space since the architectural features of the building blocks can be tailored by tuning their dimensions [9,31] and interlocking angles [25,32].

Machine Learning (ML), a branch of artificial intelligence for discerning patterns from complex datasets, enables systems to learn from existing information in order to predict new results. ML algorithms have opened a great window to the horizon of all branches of science, such as diagnosis of diseases [34], discovering drugs [35] and image recognition [36]. Recently, ML algorithms have also found their applications to material selection and exploring new material properties [37–43]. In previous studies, different ML algorithms such as deep neural networks, specifically convolutional neural networks [44,45], and generative adversarial network [46] have been used for topology optimization in order to discover new advanced materials [37,47,48]. These studies have demonstrated possible applications of ML in materials design, prediction of material/structural properties, and optimizing the functionalities and performance of advanced architectured structures.

Despite encouraging results of topologically interlocked panels in impact and energy absorption, more efforts are required to first evaluate and then optimize their performance in thermal applications. There are not sufficient studies on the thermal behavior of bioinspired brittle materials and specifically ceramics. In this study, the thermal performance of architectured ceramics with topologically interlocked designs is studied and a new approach is introduced to design architectured ceramics using a combination of finite element analysis (FEA) and ML (Figure S1 in Supporting Information). Here, a database of 400 panels from FEA is used to train a model for discovering high-performance ceramic panels. This hybrid ML-FEA model is computationally efficient for evaluating the thermal and mechanical performance of the designed architectured ceramics. The dissipation energy through friction between blocks, energy absorption and architectural failure based on safety factor are explored using finite element analysis to find high-performance architectural designs. Neural Networks are used to explore the performance of 400,000 topologically interlocked designs with distinct dimensions and interfacial angles between neighboring blocks. At the end, the designs are analyzed by finite element modelling to explore the accuracy of predictions. In Figure S1 (Supporting Information), the schematic of the design algorithm is presented.

2. Design methodology

Topologically interlocked panels [25] are built from truncated non-platonic tetrahedron ceramic blocks (see Fig. 1a). The blocks with an interlocking angle (α and β) less than 90° are contained by adjacent blocks, resulting in a topologically interlocked design. A non-regular truncated tetrahedron has two planar surfaces: a rectangle on the top and a square on the bottom (Fig. 1a). A non-regular tetrahedron is truncated unsymmetrically from top and bottom to ensure a square area with $l \times l$ dimensions on one side of truncated tetrahedron is produced. Angles on the sides AA and BB may be different (α and β in Fig. 1b). For each block two faces are tilted outward, and the other two are tilted inward. The height of the building block is set to be $h = 2.54$ mm (0.1 $inch$) and dimensions of the rectangular section is $l + 2h \times tan(\alpha)$ and $l - 2h \times tan(\beta)$. The panels with different numbers of blocks, including 3×3, 5×5 and 7×7, are considered. The overall size of the panel is set to be 10×10 cm^2. Considering two symmetry planes, the panels have 4, 6 and 8 possibilities of different interlocking angles for the 3×3, 5×5 and 7×7 structures, as reported in Table 1, respectively. Interlocking angles studied here are 5°, 10°, 15°, 20° and 25° that result in 625, 15,625 and 390,625 combinations for the 3×3, 5×5 and 7×7 panels, correspondingly. Three-dimensional displacements and rotations on all four boundaries of the panels are constrained to make fully interlocked geometries. These panels are fully constrained without using any other materials between the tiles, like adhesive. A thermal load applied to the center of the architectured panel generates transverse mechanical forces and frictional interactions between blocks. The panel also experiences an out-of-plane deformation that is distinct from the pristine ceramic panel as a baseline for comparing the thermomechanical behaviors.

(a)   (b)   (c)
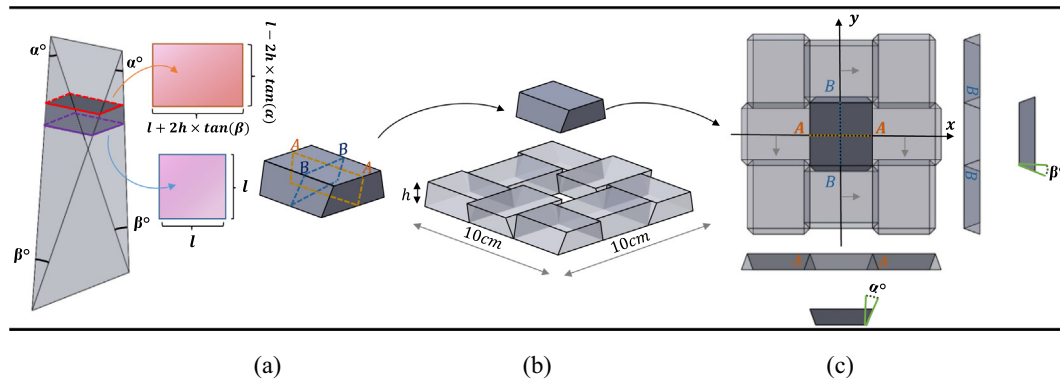
Fig. 1. Overview of the design of the topologically interlocked panel: (a) Truncated non-regular tetrahedron. (b) Block with different angles in *AA* and *BB* surfaces and the locking configuration of adjacent blocks in the 3 × 3-block panels. (c) Symmetry planes in the architectured panel and different angles of blocks on each side (α, β).

Table 1
All possible architectured designs by changing the angles between blocks. Each color represents an angle (α, β).

| Number of blocks	Interlocking angles (α, β)	Number of designs with alternative interlocking angles	Arrangement
3 × 3	5°, 10°, 15°, 20°, 25°	$5^4 = 625$	
5 × 5	5°, 10°, 15°, 20°, 25°	$5^6 = 15625$	
7 × 7	5°, 10°, 15°, 20°, 25°	$5^8 = 390625$	

3. Finite element analysis

FEA is performed using ANSYS Workbench 2019 R3 on panels with different numbers of building blocks and interlocking angles. Panels with the 3 × 3 (9), 5 × 5 (25) and 7 × 7 (49) arrays of blocks as well as 5°, 10°, 15°, 20° and 25° interlocking angles are considered. The architectured designs have two symmetry planes, one normal to the *x*-direction and one normal to the *y*-direction (see Fig. 1c). Material properties of non-porous alumina ceramics are assumed to be isotropic linear elastic. Different properties of the alumina ceramics are listed in Supporting Information, Table S1 [9]. These properties are considered constant in the range of temperature analysis. Transient thermal analysis is first performed to evaluate the thermal performance of different architectured designs. A constant temperature (i.e., thermal load) is applied to a circular area with a radius of 10 *mm* in the middle of the panel. The rest of the panel containing edges is exposed to free convection with a heat transfer coefficient of 10 $\frac{W}{m^2K}$. Due to the fixed boundaries in peripheral blocks, the thermal expansion of the panel

results in in-plane forces between building blocks. A thermomechanical study is performed to explore the mechanical behavior of the panels under the thermal load. Coulomb-Mohr failure criterion (see Eq. (1)) for brittle materials is employed to evaluate the safety factor (*SF*) of each design, which is the minimum of the safety factor of all material points in the architectured ceramic [49]:

$$SF = min \left(\begin{cases} \frac{S_t}{\sigma_1} & \sigma_1 \geq \sigma_3 \geq 0 \\ \frac{S_t}{\sigma_1 - \frac{S_t}{S_c}\sigma_3} & \sigma_1 \geq 0 \geq \sigma_3 \\ \frac{S_c}{\sigma_3} & 0 \geq \sigma_1 \geq \sigma_3 \end{cases} \right) \qquad (1)$$

where the maximum and minimum principal stresses are represented by σ_1 and σ_3; S_t and S_c are tensile and compressive ultimate strength, respectively. As shown in Fig. 2, the temperature in the circle with a radius of 10 *mm* in the middle of the panels is increased to 700 °C in 60 s then the middle circle area is kept at 700 °C for 540 s; 700 °C is picked for the maximum temperature
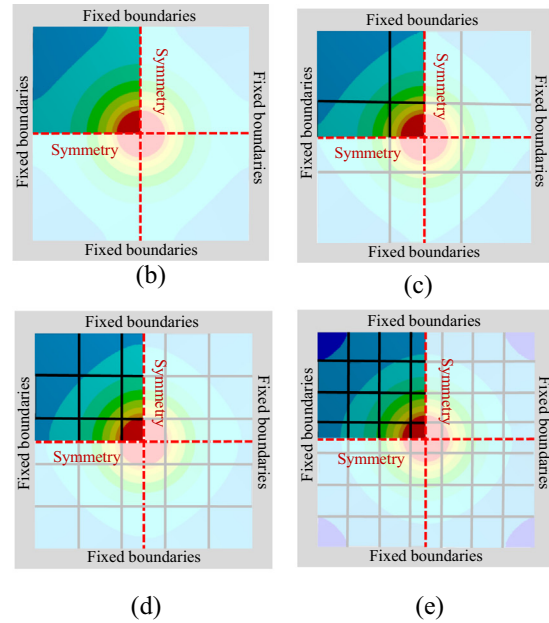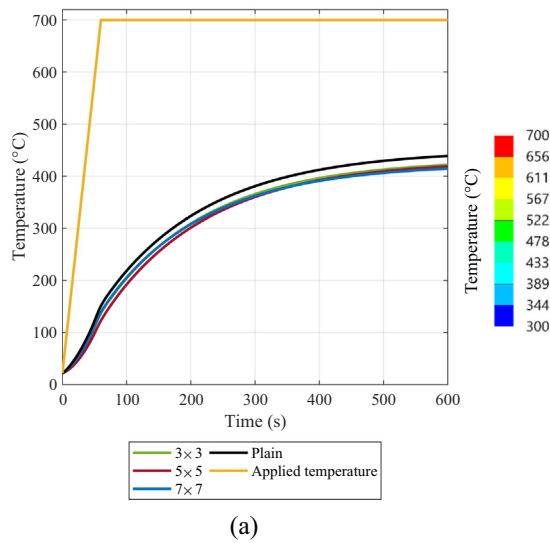
Fig. 2. Temperature response of ceramic panels: (a) Transient temperature variation; Temperature distribution at the end of the analysis (t = 600 s) for (b) Plain and architectured panels with (c) 3 × 3, (d) 5 × 5 and (e)7 × 7 arrays of blocks.

since the average safety factor in this condition lies between 1 and 2. This transient thermal analysis is done within 600 s. The input and output energies of the system are equal at 600 s and the whole panel reaches a steady-state condition. Identical temperature distributions for the panels with 3 × 3, 5 × 5 and 7 × 7 arrays of blocks are observed as each block is perfectly in contact with adjacent blocks (Fig. 2b to 2e). Mesh sensitivity is conducted to assure the reliability of the FEA. The majority of the architectued panle has been discretized by Hex dominant mesh element type, while the middle panel experiencing contact has descetized by Tetrahedral mesh. The maximum mesh size is set to be 10^{-3} m over the whole panel, except in contact area where the maximum mesh size is selected as 8×10^{-4} m. Therefore, the small amount of temperature difference in Fig. 2a (1–2 °C) is due to the gaps generated to geometries of building blocks where some materials between corners of blocks are removed to achieve interlocking designs. Material removal is causing less than 0.9% difference in the volume of structures due to the gaps.

Temperature distribution causes distinct thermal expansion at different locations of the panels; for example, the middle tile is exposed to a higher temperature that leads to a higher out-of-plane deflection compared to the others. The out-of-plane deflection is due to in-plane deformation caused by a combination of sliding, thermal buckling and bending. The in-plane thermal stress has been computed by importing the determined temperature distribution to the mechanical module of ANSYS Workbench. The static coefficient of friction between ceramic blocks is set at 0.24 [25]. Different thermal expansion of adjacent tiles causes sliding and energy dissipation through contact. Displacements in all three directions of x, y and z are fixed on all four edges of the ceramic panels and the temporal behavior of the panels is studied. Energy balance is calculated to observe the mechanical performance of the panels [50]:

$$U = Q + W_t \tag{2}$$

$$W_t = E_{strain} + E_{FDE} + W_{env} \tag{3}$$

where U, Q and W_t are internal energy, thermal energy and mechanical energy, respectively. E_{strain}, E_{FDE} and W_{env} are strain energy, frictional dissipation energy (FDE) and work on the environment, respectively. Thermal energy stored in the system is determined by the specific heat of alumina ceramic. To compute the internal and thermal energy of the system, ANSYS Fluent is used. At $t = 600$ s, inlet and outlet of the internal energy of the system are equal and 8.71 kJ energy is stored as internal energy. This 8.71 kJ is separated into thermal energy $Q = 8.58$ kJ (98% of total internal energy) and mechanical energy as $W_t = 0.13$ kJ that consists of three parts: (1) Strain energy that is the mechanical energy stored in the system, (2) Frictional dissipation energy and (3) Work on the surrounding environment by deflection of the architectured panel. Mechanical energy is calculated by fixing the whole of the plain panel and setting the displacements in all three directions equal to zero. In this approach, the mechanical energy is equal to the strain energy of the panel as W_{env} and E_{FDE} is set equal to zero. The total amount of energy received by all designed architectured panels is the same, leading to equal thermal energy and mechanical energy for all panels. However, strain energy (E_{strain}), frictional dissipation energy (E_{FDE}), and work on the surrounding environment (W_{env}) vary for alternative designed architectures.

4. Machine learning (ML)

ML is an application of artificial intelligence and a data-driven approach to find a pattern in existing data. In this work, ML is used to examine the thermomechanical performance of a series of alternative architectured ceramic panels. Interlocking angles and the number of blocks are inputs, while safety factor, max deflection, sliding distances, reaction forces on the boundaries, frictional dissipation and strain energies are outputs of the model. Fig. 3 represents the schematic of the whole algorithm. For each of the 3 × 3, 5 × 5 and 7 × 7-block architectured panels, 100 random designs have been analyzed by FEA. Interlocking angles in the designs are varied from 5° to 25°. The correlation of input parameters to outputs is investigated in the preprocessing step. Normalizing and
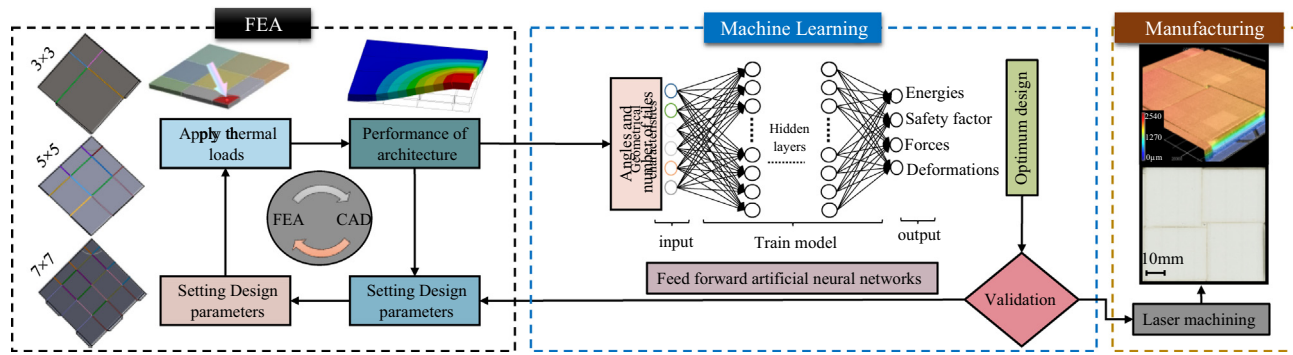
Fig. 3. Schematic of the algorithm for studying the thermomechanical performance of architectured materials. By varying interlocking angles from 5° to 25°, 406,875 different architectured panels can be produced, which are studied by a Neural Network algorithm.

scaling help the ML models to converge and make the training less sensitive to the scale of features.

Middle architectured ceramic blocks interact with four surrounding blocks, while blocks on edges and corners interact with two or three blocks, respectively. The vast design space (Table 1) is computationally expensive to be modelled only by using FEA; ML algorithms can assist in exploring all possible designs. Multilayer perceptron (MLP), as a class of feedforward artificial neural network (ANN) for the regression problem [51] is employed due to its better performance compared to other models [52] (Supporting Information 3 and 4). For this purpose, MLP regressor from Sklearn library is used in Python. Hyperparameters such as the number of hidden layers, the L2 penalty parameter, the initial value for learning rate and the max number of iterations are tuned by conducting a grid search. ReLu activation function has been used due to its higher accuracy than the logistic activation function. ReLu activation outputs directly the positive input and outputs the negative input to zero [53,54]. Randomly, 10% of the dataset is picked for the test set and five-fold cross-validation is chosen to prevent overfitting. The mean accuracy of the ML models for predicting each output are reported in Table 2.

5. Results and discussion

In this section, the effects of interlocking angles on the thermomechanical response of architectured ceramic panels are studied. All boundary conditions and thermal loads remained unchanged for the sake of comparison of the performance of alternative architectured ceramics. First, we compare the responses when all blocks have identical interlocking angles. Then, ML algorithms are used to investigate all possible panels that have building blocks with dissimilar interlocking angles.

Fig. 4 presents safety factors, reaction forces on boundaries and strain for plain and architectured (10° interlocking angle) ceramic panels during a time span of 600 s. While the plain ceramic panel fails after 50 s, all the architectured panels remain integrated over the period of the time considered. A higher amount of strain energy inside the plain panel and higher reaction forces on fixed boundaries are observed, resulting in a rapid failure compared to the architectured ceramic. Meanwhile, for this architectured design, about 3% of the mechanical energy is dissipated through sliding and friction in the constitutive building blocks. The energy dissipation assists the architectured panels to resist the same thermal load in a larger time frame. The 7 × 7-block architectured panel with uniform distribution of interlocking angle 10° presents a higher safety factor compared to the 3 × 3 and 5 × 5-block architectured panels. Architectured ceramic panels with alterna-

tive interlocking angles are explored in the next section to ensure the accuracy of the comparison of the thermomechanical performance of panels. It can be concluded that the plain panel performs poorly compared to the designed architectures in terms of failure resistance, the application of higher forces on the boundaries and the development of higher strain energy.

5.1. Architectured designs with uniform interlocking angles

Architectured panels with a uniform distribution of interlocking angles are studied here. The analysis considers all blocks having the uniform interlocking angles; however, they can be varied from 5° to 25°. In Fig. 5, strain energy, frictional dissipation energy (FDE), reaction force and out-of-plane deformation are presented. As seen in Fig. 5a, the values of FDE are negligible for interlocking angles of less than 10°. At 10° interlocking angle, FDE starts to increase and a drop is observed in the strain energy, indicating that the sliding begins at 10°. Frictional sliding mechanism is one of the key factors to have better resistance to failure. Stresses and energies inside the panels are reduced when more energy is dissipated through friction. For interlocking angles larger than 15°, FDE in the 3 × 3-block panel is higher and consequently, its average safety factor is higher than the 5 × 5 and 7 × 7-block panels.

In general, less strain energy in the panels results in a lower reaction force on the boundaries. As shown in Fig. 5c, for the interlocking angles between 15° and 30°, the 3 × 3-block panel has a lower force on the boundaries and a higher safety factor compared to the other panels. Out-of-plane deformation of the panels (Fig. 5b) with interlocking angles more than 15° is less than their counterparts with lower interlocking angles. At 10°, a drop in the out-of-plane deformation is observed because the panel experiences a locking behavior that hinders blocks from being deformed. This trend is different for the 5 × 5-block architectured panels because the deflection depends on the area where the temperature is applied (a circle with a diameter of 10 mm that is ~3% of the total area of the top surface). Except the 3 × 3-block panel, the heat is applied to more than 1 block. As expected for the higher interlocking angles, more sliding occurs as shown in Fig. 5d. The results show that the sliding distance, which represents the sum of the path of the movement, is highly correlated to the panel safety factor. Even though the 3 × 3-block architectured panel has less contact areas, this panel reveals more sliding and a higher safety factor. Higher sliding is a representation of dissipating more energy, the energy that can be stored in the panel causing stress inside the panel. In the next section, ML algorithms are adopted to explore the dependence of the architectures with variable angles on the outputs.
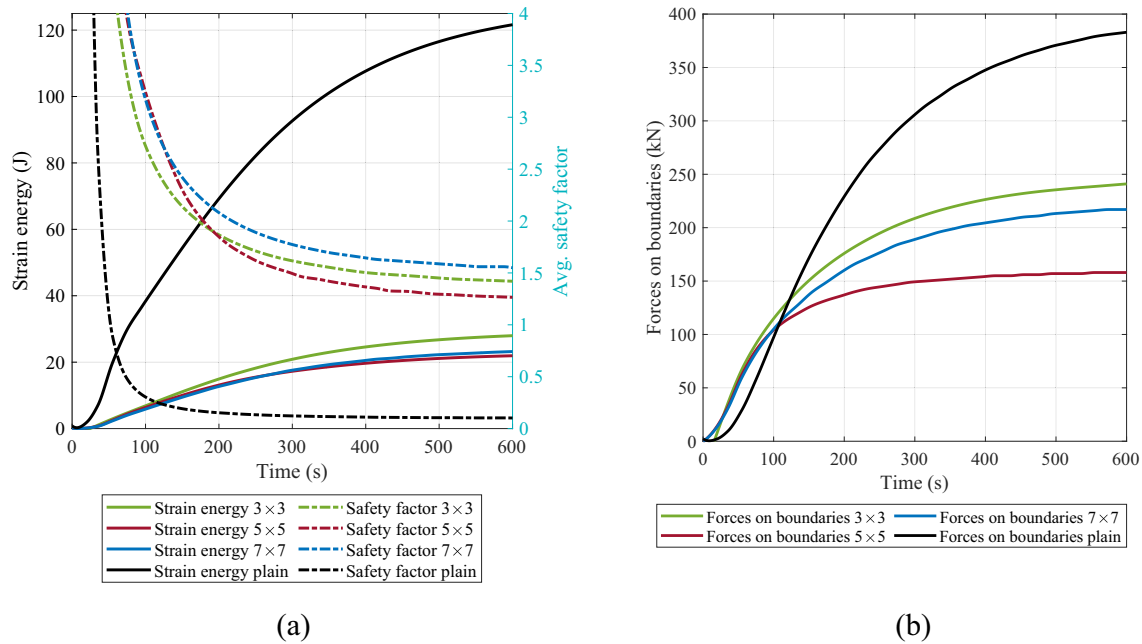
Fig. 4. (a) Comparing strain energy and safety factor of the architectured panels with the plain one. The plain panel fails earlier than the architectured designs, and it suffers from a higher amount of stress inside the panel. (b) Comparing reaction forces on fixed boundaries of the architectured panels with the plain one. The plain panel applies higher forces to the fixed boundaries.

### 5.2. Exploring designs with variable angles using machine learning

Data from FEA is imported to ML models to find better-performing architectured panels with respect to each output (e.g. strain energy and out-of-plane deformation). These panels are made concerning the accuracies presented in Table 2. To enhance the quality of data, preprocessing has been done over ML models. The preprocessing includes determining the correlation of each interlocking angle to output, which shows some of the interlocking angles in designs have a small correlation to the outputs. Low correlation can reduce the accuracy of the ML models. Exploring correlation indicates that some of the interlocking angles do not affect outputs; for example, the interlocking angle 2 (A_2) has a negligible correlation to the FDE of the 3×3-block architectured panel. These slightly correlated angles are removed in the training process as identified as θ in Table 2. Different numbers of building blocks as inputs need three different ML models (see Section 4) with specific hyperparameters to be developed. In Fig. 6, correlations between inputs and outputs are shown in different designs. It is observed that interlocking angles in structures with a higher number of building blocks have less correlation to the outputs (Fig. 6e and 6f). This can be addressed by having a small amount of training data for the 7×7-block panel compared to the 3×3-block panel.

Highly correlated parameters can reveal great information about which interlocking angles should be controlled in each architectured panel. For example, all four interlocking angles in the 3×3-block panel have a higher negative correlation to the total strain energy over the whole panel, suggesting small interlocking angles bring a higher amount of strain energy. Maximum and minimum strain energies, safety factor, total frictional dissipation through contacts, sliding distances, out-of-plane deformation and reaction force on boundaries are presented. ML algorithms suggest a series of designs that can achieve maximum or minimum of the aforementioned outputs. In this regard, panels with more similar

interlocking angles are selected since they are more favorable in terms of manufacturing [55][56] (see Figure S6). Some interlocking angles have a small impact on the output because of that any values can be picked for those angles with θ in Table 2.

Panels with a greater number of inputs need more data to predict accurately. The mean accuracy for the output parameters in the 7×7-block architectured panel is much less than the 3×3 and 5×5-block panels; this indicates that training a model for the 7×7-block panel is more challenging than the other architectured panels.

Here, we explore the accuracy of predicted output values by ML through comparison with the FEA results. In Fig. 7, the performance of the suggested varied-angle architectured panels from ML is compared with the FEA results for the architectured panels with uniform interlocking angles across the panel. The maximum and minimum values of the outputs are reported in Fig. 7. In most cases, ML could increase the maximum and decrease the minimum of outputs. However, ML could not increase the maximum out-of-plane deformation and FDE in the 7×7-block architectured panel due to the low amount of training data. The deformations and FDE in the 3×3 and 5×5-block panels can be increased by using ML and designing varied-angle architectured panels. In the 3×3-block panel, 15%, 7% and 30% improvements in maximum out-of-plane deformation, sliding distance and frictional dissipation energy are observed, respectively. In addition, 70%, 80% and 30% reductions in the minimum out-of-plane deformation, sliding distance, and frictional dissipation energy are observed, respectively. In the 5×5-block panel, 3%, 35% and 4% improvements in maximum out-of-plane deformation, sliding distance and FDE are observed, respectively. In addition, 70%, 15% and 52% reductions in minimum out-of-plane deformation, sliding distance and FDE are observed in the results, respectively. ML is not providing new designs to maximize or minimize the force on the boundaries, strain energy, and safety factor.

(a)

(b)
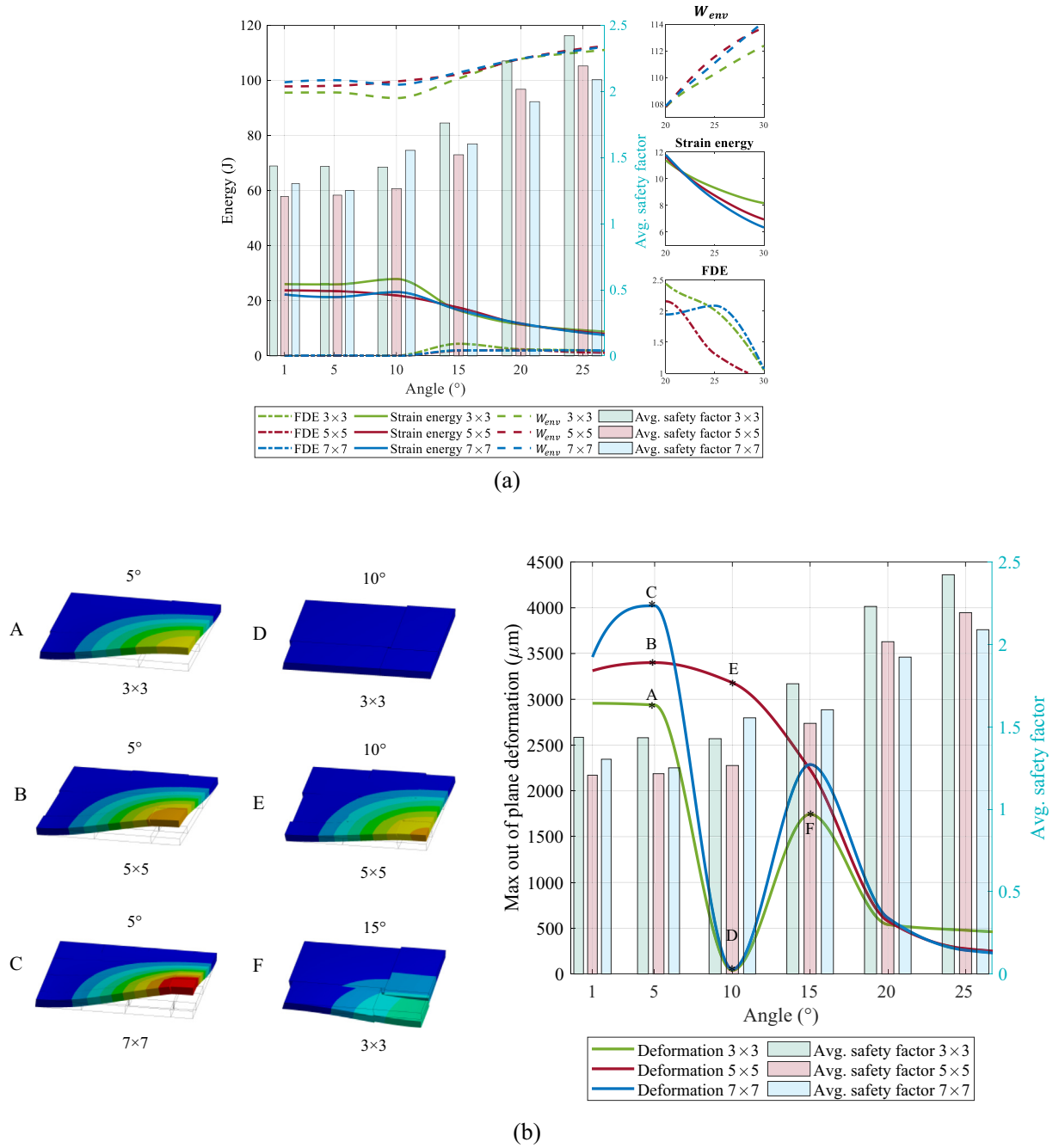
Fig. 5. Comparing the performance of architectured designs with the uniform distribution of the interlocking angles: (a) Energy comparison and safety factor, (b) Out-of-plane deformation, (c) Force reaction on fixed boundaries and (d) Total sliding distance of adjacent blocks over the whole of the architectured panel.

5.3. Validation

Proposed designs from the ML algorithms are explored by FEA in Fig. 8 to further validate the ML predictions. For this purpose, three representative designs and associated outputs, which are FDE and sliding distance in the 3×3-block architectured panel and out-of-plane deformation in the 5×5-block architectured panel, are chosen from Table 2 (bolded) to be investigated.

To achieve the maximum FDE for varied-angle architectured panels of 3×3, ML suggested selecting angle $1(\alpha) = 15°$, angle $3(\gamma) = 20°$ and angle $4(\delta) = 15°$. Interlocking angle $2(\beta)$ in

this design can be varied due to a small correlation to the frictional dissipation energy (FDE). Fig. 8b indicates the effect of changing interlocking angle $2(\beta)$ on the frictional dissipation energy of the architectured panel. This horizontal blue line indicates that interlocking angle $2(\beta)$ does not play a significant role in the maximization of FDE. To validate the results of ML for varied-angle architectured panels, a second round of FEA is conducted. In Fig. 8b and 8c the red points are representation of FEA results of varied-angle designs suggested by ML. Maximum 5% difference is observed in results from ML and FEA for varied-angle panels. The horizontal blue line associated with ML varied-angle architectured
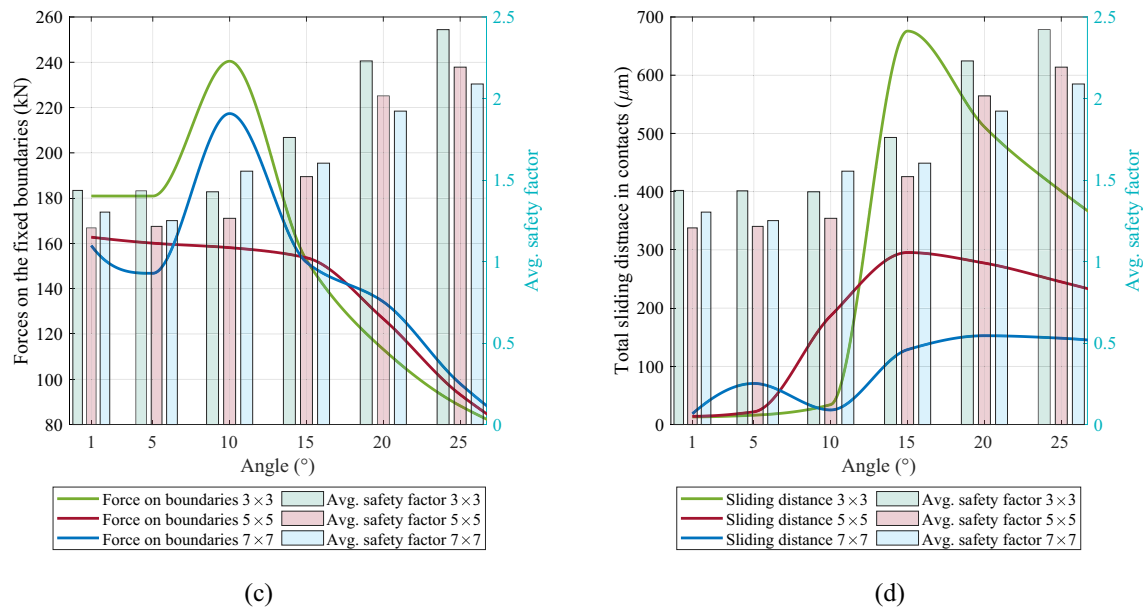
(c)

(d)

Fig. 5 (*continued*)

Table 2
ML algorithms for the architectured ceramic designs with the minimum and maximum outputs. Each output and the mean accuracy for each model are reported.

3 × 3-block panel	A_1	A_2	A_3	A_4	A_5	A_6	A_7	A_8	Mean accuracy (%)	R^2 error
Max strain energy	5°	5°	5°	5°	–	–	–	–	84	0.96
Min strain energy	25°	25°	25°	25°	–	–	–	–		
Max deformation	5°	5°	25°	15°	–	–	–	–	73	0.77
Min deformation	25°	25°	5°	25°	–	–	–	–		
Max avg. safety factor	25°	25°	25°	25°	–	–	–	–	94	0.95
Min avg. safety factor	5°	5°	5°	25°	–	–	–	–		
Max total FDE	**15°**	**θ**	**20°**	**15°**	–	–	–	–	65	0.32
Min total FDE	5°	θ	5°	5°	–	–	–	–		
Max total sliding distance	**15°**	**20°**	**θ**	**10°**	–	–	–	–	72	0.93
Min total sliding distance	5°	5°	θ	5°	–	–	–	–		
Max force on the boundaries	5°	5°	15°	5°	–	–	–	–	74	0.94
Min force on the boundaries	25°	25°	25°	25°	–	–	–	–		

5 × 5-block panel	A_1	A_2	A_3	A_4	A_5	A_6	A_7	A_8	**Mean accuracy (%)**	R^2 **error**
Max strain energy	5°	5°	5°	5°	5°	5°	–	–	85	0.71
Min strain energy	25°	25°	25°	25°	25°	25°	–	–		
Max deformation	**5°**	**25°**	**5°**	**25°**	**5°**	**5°**	–	–	86	0.70
Min deformation	25°	5°	25°	5°	25°	25°	–	–		
Max avg. safety factor	25°	5°	25°	5°	25°	25°	–	–	85	0.88
Min avg. safety factor	5°	5°	5°	5°	5°	5°	–	–		
Max total FDE	25°	5°	5°	5°	5°	5°	–	–	60	0.85
Min total FDE	5°	25°	25°	25°	5°	25°	–	–		
Max total sliding distance	5°	25°	5°	θ	25°	25°	–	–	71	0.32
Min total sliding distance	5°	5°	5°	θ	5°	5°	–	–		
Max force on the boundaries	5°	5°	5°	5°	5°	5°	–	–	70	0.89
Min force on the boundaries	25°	25°	25°	25°	25°	25°	–	–		

7 × 7-block panel	A_1	A_2	A_3	A_4	A_5	A_6	A_7	A_8	**Mean accuracy (%)**	R^2 **error**
Max strain energy	5°	5°	25°	5°	25°	5°	5°	25°	60	0.62
Min strain energy	25°	15°	15°	25°	20°	25°	25°	15°		
Max deformation	5°	25°	25°	5°	θ	5°	5°	θ	67	0.36
Min deformation	5°	5°	5°	5°	θ	25°	25°	θ		
Max avg. safety factor	25°	25°	25°	25°	5°	25°	25°	5°	80	0.71
Min avg. safety factor	5°	5°	5°	5°	5°	5°	5°	5°		
Max total FDE	5°	25°	5°	25°	θ	25°	25°	θ	54	0.13
Min total FDE	25°	5°	20°	5°	θ	5°	5°	θ		
Max total sliding distance	25°	θ	5°	θ	5°	25°	θ	25°	57	0.13
Min total sliding distance	25°	θ	25°	θ	25°	10°	θ	5°		
Max force on the boundaries	5°	5°	25°	25°	5°	θ	25°	25°	75	0.58
Min force on the boundaries	20°	15°	5°	5°	25°	θ	20°	5°		

Bolded text represents the structures that have been further investigated by FEA.
θ represents the angles that have a small correlation to the outputs.
A_1-A_8 represent the angles that are shown in Fig. 6.
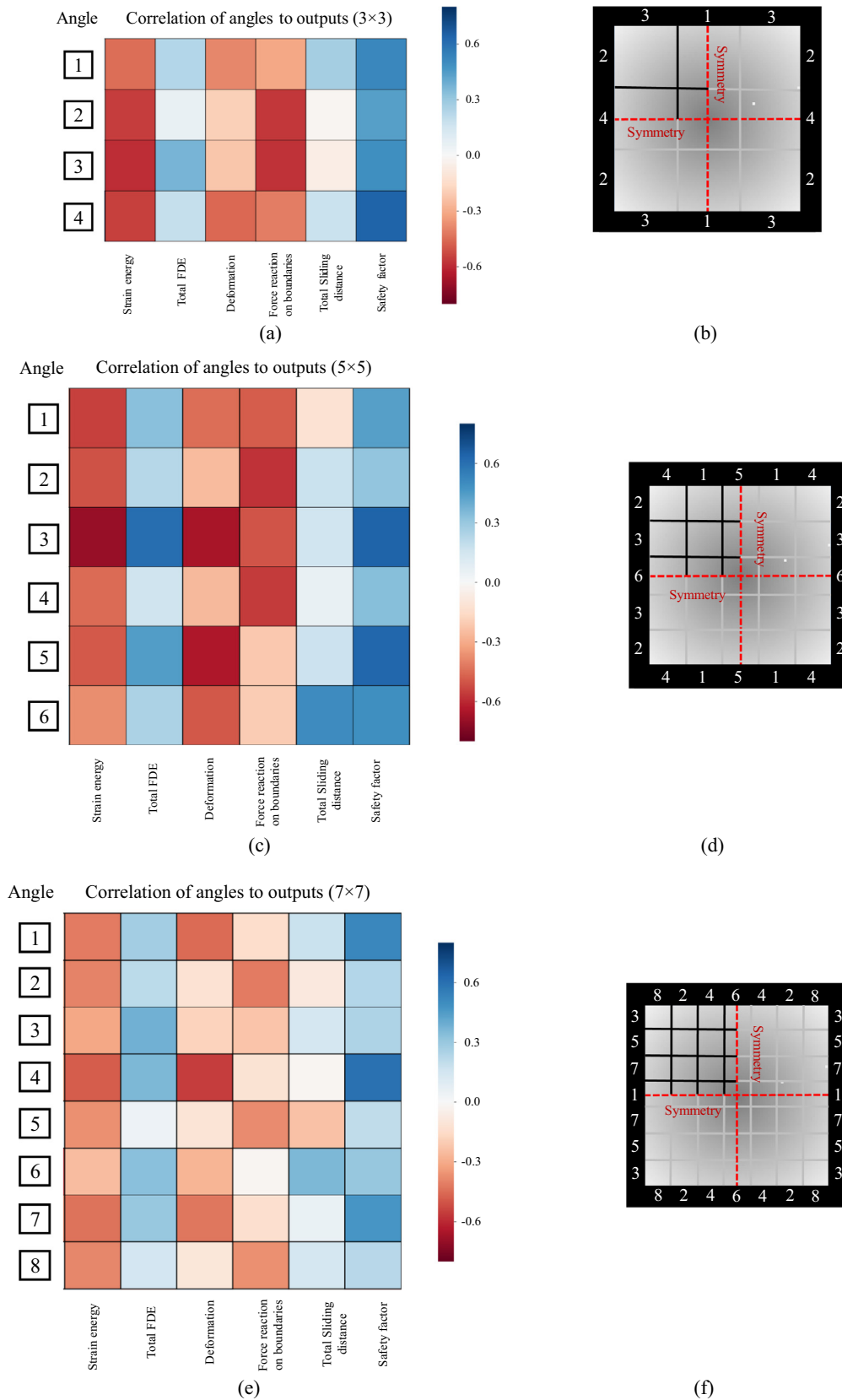
Fig. 6. (a, c, e) Correlation between input parameters as interlocking angles and output parameters. Schematic of (b) 3 × 3-block architectured panel, (d) 5 × 5-block architectured panel, (f) 7 × 7-block architectured panel and symmetry planes. Each number represents a different interlocking angle.
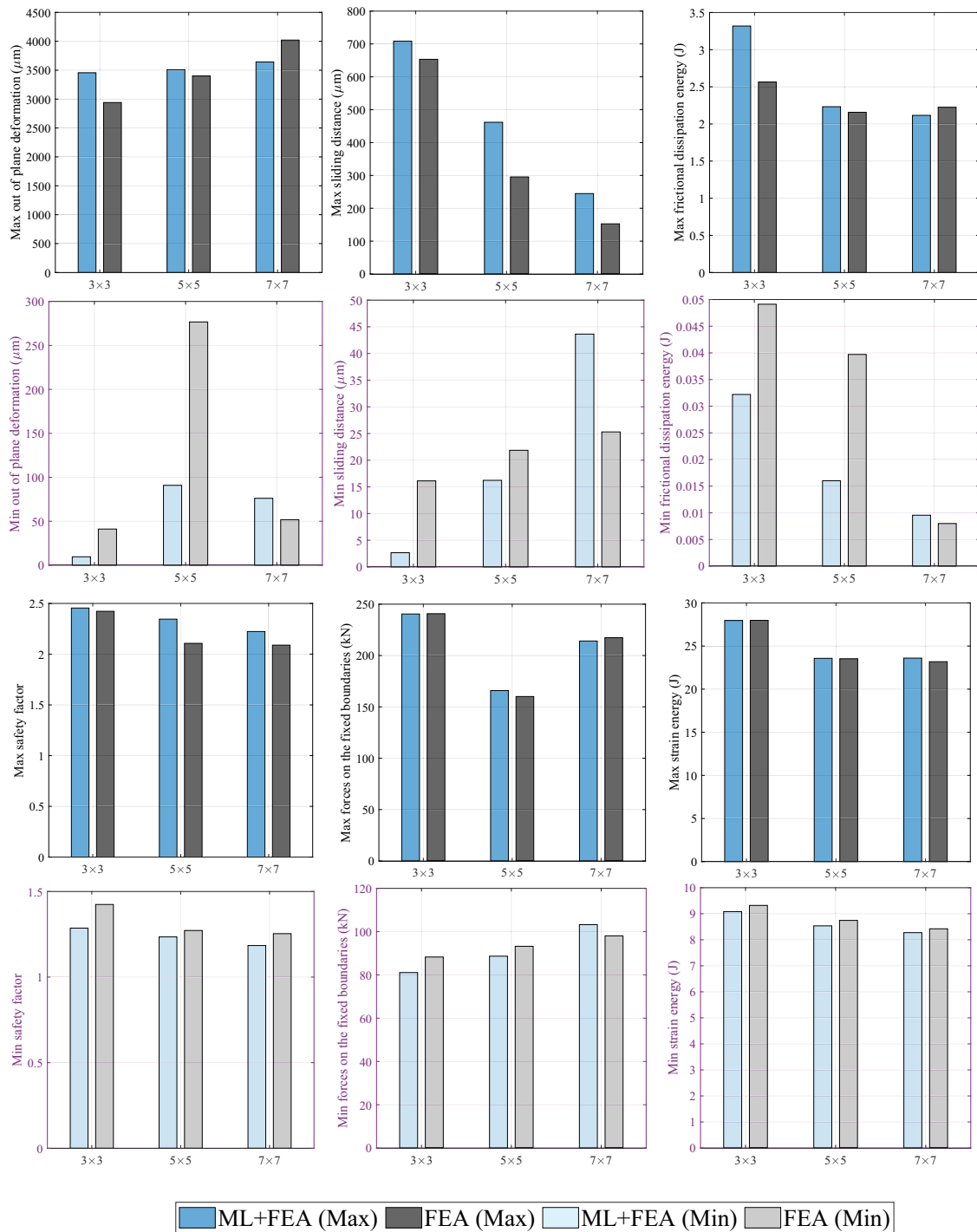
Fig. 7. Comparison of predicted results from ML with results directly from FEA. Min and Max in these figures represent mimimum and maximum of the corresponding results.

panels is higher than the black line associated with the uniform-angle design. This indicates that the varied-angle architectured panels, found by ML and validated by FEA, lead a higher maximum FDE. The same reasoning can be used for the sliding distance and the varied-angle architectured panel with $\alpha = 15^\circ$, $\beta = 20^\circ$,

γ and $\delta = 10^\circ$ (see Fig. 8c). In Fig. 8d, the out-of-plane deformation of the varied-angle architectured panel with the 5×5 arrays of blocks is compared with the uniform-angle panel. It is shown that the maximum out-of-plane deformation of the 5×5-block architectured panel is 3% increased for the varied-angle panel.
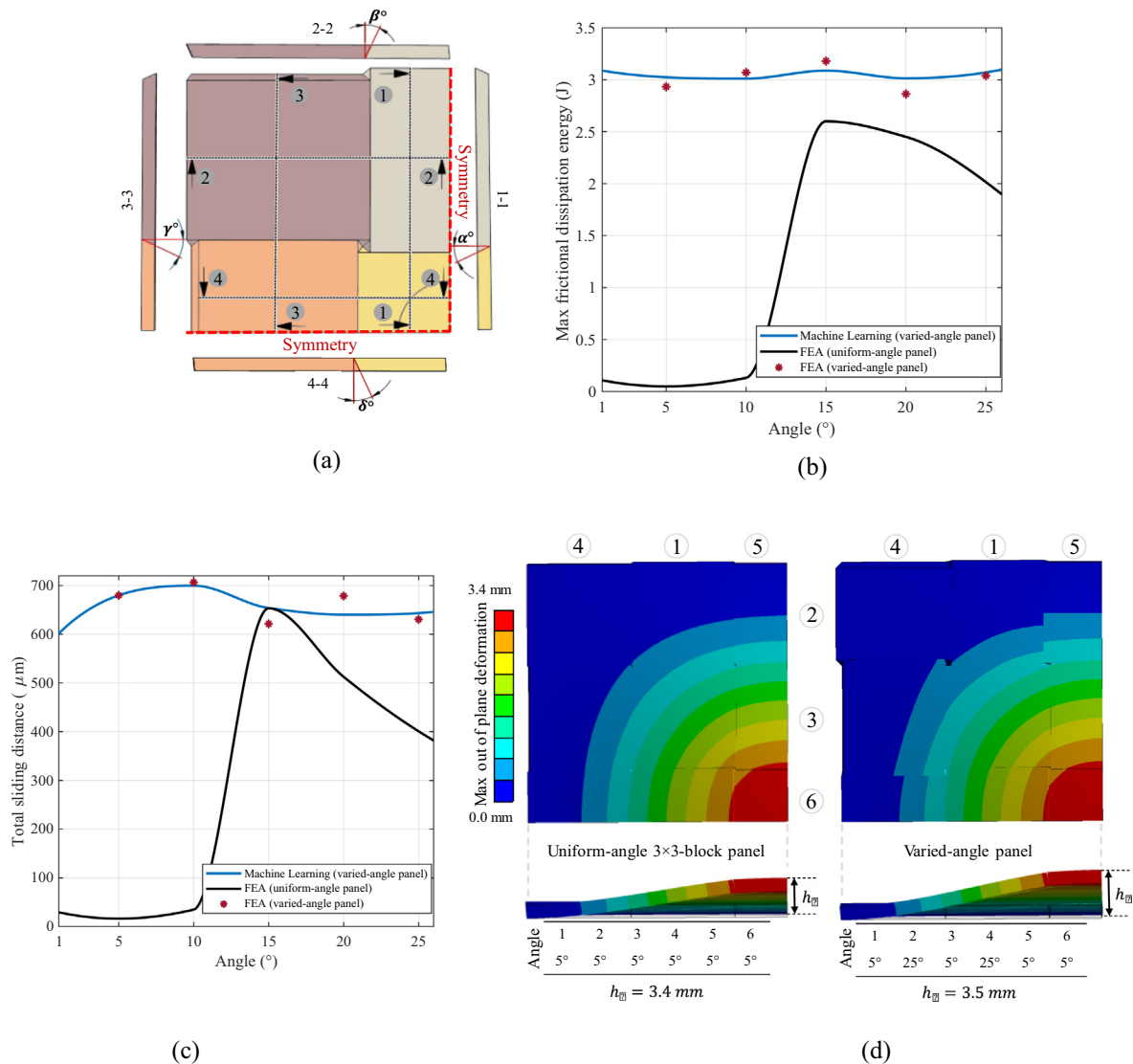
Fig. 8. Comparison of the varied-angle and uniform-angle architectured panels. (a) Schematic of 3×3-bock panel with varied-angle; $\alpha = angle1$, $\beta = angle2$, $\gamma = angle3$, $\delta = angle4$. (b) ML-assisted varied-angle panel design to maximize FDE; $\alpha = 15°$, β, $\gamma = 20°$, $\delta = 15°$. The ML-assisted results, validated by FEA, for the varied-angle design are shown in the blue line. (c) The suggested varied-angle panel, $\alpha = 15°$, $\beta = 20°$, γ, $\delta = 10°$, to maximize the sliding distance. (d) Comparison of maximum out-of-plane deformation in the 5×5-block architectured panels with the varied-angle and uniform-angle designs. (For interpretation of the references to color in this figure legend, the reader is referred to the web version of this article.)

6. Concluding remarks

Despite the excellent thermal stability of ceramics, most of the research endeavors have focused on evaluating the mechanical performance of ceramics under quasi-static or impact loading rather than a thermal stimulus. In this study, FEA is used to evaluate the thermomechanical performance of architectured ceramics made of interlocked building blocks. It is shown that the architectured designs outperform monolithic ceramics in the energy dissipation, resulting in a 67% reduction in forces on the fixed boundaries and a 90% increase in the safety factor. We have proposed a systematic approach by adopting a hybrid ML-FEA algorithm to design high-performance architectured ceramics experiencing thermal loads. In this analysis, the out-of-plane deformation, strain and frictional dissipation energies, reaction forces, safety factor and sliding distances of adjacent blocks in the architectured ceramics made of interlocked building blocks are explored. MLP algorithm is used to find the designs with maximum and minimum outputs by changing the angle of cuts

between the building blocks. It is shown that the suggested designs by ML-FEA algorithms perform better for the desired outputs. For instance, these designs can dissipate 30% more energies through friction and 7% more energies sliding between blocks compared to the interlocked architectures with constant cutting angles. It is demonstrated that the architectured ceramic panels perform better in a thermomechanical environment compared to the monolithic ceramics. ML tool is computationally efficient to conduct a parametrical study to explore the effects of the architectural parameters on multifunctional performance of architectued matrials. ML algorithms can predict desired outputs, 300 times faster than using finite element software, making the search for high-performance architectured materials possible in a vast design space. Once the ML model is properly trained, it can predict numerical results without an access to a commercial FEA software that is of substantial importance in material design and optimization.

In this algorithm, ML results are investigated by conducting a second round of FEA. Maximum 5% error was found in the results from FEA and ML in the validation process. Although this error

can be acceptable but increasing number of parameters in the design algorithm will increase the error.

Instead of using FEA data for training ML algorithms, there is a possibility to also use both experimental and FEA data to increase the accuracies. In future studies, experimental data can be produced by employing a laser cutting technique to experimentally validate the numerical and ML-assisted predictions (see Supporting Information, Figure S6 [8,55]). The novel paradigm offered by advanced additive/subtractive manufacturing along with ML tools can facilitate the development of advanced ceramic materials that can prevail material property tradeoffs found in monolithic materials (e.g. toughness in brittle materials). This work not only provides a new method that harnesses simulation data and ML to design future bioinspired, architectured and composite materials in an experience-free and systematic manner, but also opens a new avenue to address various inverse design problems in different industrial sectors such as aerospace, automotive, transportation and energy.

Declaration of Competing Interest

The authors declare that they have no known competing financial interests or personal relationships that could have appeared to influence the work reported in this paper.

Acknowledgments

Data availability

The data required to reproduce these findings cannot be shared at this time as the data also forms part of ongoing studies.

Appendix A. Supplementary material

Supplementary data to this article can be found online at https://doi.org/10.1016/j.matdes.2021.110056.

References

[1] T.G. King, M.E. Preston, B.J.M. Murphy, D.S. Cannell, Piezoelectric Ceramic Actuators - a Review of Machinery Applications, Precis. Eng.-J. Am. Soc. Precis. Eng. 12 (3) (1990) 131–136.

[2] R.P. Schmidt, Aircraft thermal protection system, Google Patents, 1996.

[3] S.J. Kalita, A. Bhardwaj, H.A. Bhatt, Nanocrystalline calcium phosphate ceramics in biomedical engineering, Mater. Sci. Eng. C-Biomim. Supramol. Syst. 27 (3) (2007) 441–449.

[4] B.S. Bal, M.N. Rahaman, Orthopedic applications of silicon nitride ceramics, Acta Biomater 8 (8) (2012) 2889–2898.

[5] J.F. Shackelford, Bioceramics: Applications of ceramic and glass materials in medicine, Trans Tech Publications, Switzerland, 1999.

[6] A.G. Evans, Perspective on the development of high-toughness ceramics, J. Am. Ceram. Soc. 73 (2) (1990) 187–206.

[7] J. Justin, A. Jankowiak, Ultra High Temperature Ceramics: Densification, Propert. Therm. Stabil. (2011).

[8] C. Beausoleil, H. Yazdani Sarvestani, Z. Katz, J. Gholipour, B. Ashrafi, Deep and high precision cutting of alumina ceramics by picosecond laser, Ceram. Int. 46 (10) (2020) 15285–15296, https://doi.org/10.1016/j.ceramint.2020.03.069.

[9] H. Yazdani Sarvestani, M. Mirkhalaf, A.H. Akbarzadeh, D. Backman, M. Genest, B. Ashrafi, Multilayered architectured ceramic panels with weak interfaces: energy absorption and multi-hit capabilities, Mater. Des. 167 (2019), https://doi.org/10.1016/j.matdes.2019.107627 107627.

[10] H. Yazdani Sarvestani, C. Beausoleil, M. Genest, B. Ashrafi, Architectured ceramics with tunable toughness and stiffness, Extreme Mech. Lett. 39 (2020), https://doi.org/10.1016/j.eml.2020.100844 100844.

[11] K. Liu, L. Jiang, Multifunctional integration: from biological to bio-inspired materials, ACS Nano 5 (9) (2011) 6786–6790.

[12] U.G.K. Wegst, H. Bai, E. Saiz, A.P. Tomsia, R.O. Ritchie, Bioinspired structural materials, Nat Mater 14 (1) (2015) 23–36.

[13] M.A. Meyers, A.Y.M. Lin, Y. Seki, P.-Y. Chen, B.K. Kad, S. Bodde, Structural biological composites: An overview, Jom 58 (7) (2006) 35–41.

[14] C. Zhang, D.A. Mcadams, J.C. Grunlan, Nano/Micro-Manufacturing of Bioinspired Materials: a Review of Methods to Mimic Natural Structures, Adv. Mater. 28 (30) (2016) 6292–6321.

[15] Z. Jia, Y. Yu, L.F. Wang, Learning from nature: Use material architecture to break the performance tradeoffs, Mater. Des. 168 (2019) 107650.

[16] Q. Cheng, L. Jiang, Z. Tang, Bioinspired layered materials with superior mechanical performance, Acc. Chem. Res. 47 (4) (2014) 1256–1266.

[17] S.E. Naleway, M.M. Porter, J. McKittrick, M.A. Meyers, Structural Design Elements in Biological Materials: Application to Bioinspiration, Adv. Mater. 27 (37) (2015) 5455–5476.

[18] M.A. Meyers, P.-Y. Chen, A.-M. Lin, Y. Seki, Biological materials: structure and mechanical properties, Prog. Mater Sci. 53 (1) (2008) 1–206.

[19] F. Barthelat, Architectured materials in engineering and biology: fabrication, structure, mechanics and performance, Int. Mater. Rev. 60 (8) (2015) 413–430.

[20] N.A. Fleck, V.S. Deshpande, M.F. Ashby, Micro-architectured materials: past, present and future, Proc. Roy. Soc. a-Math. Phys. Eng. Sci. 466 (2121) (2010) 2495–2516.

[21] S. Rudykh, C. Ortiz, M.C. Boyce, Flexibility and protection by design: imbricated hybrid microstructures of bio-inspired armor, Soft Matter 11 (13) (2015) 2547–2554.

[22] Z. Yin, F. Hannard, F. Barthelat, Impact-resistant nacre-like transparent materials, Science 364 (6447) (2019) 1260–1263.

[23] L. Djumas, G.P. Simon, Y. Estrin, A. Molotnikov, Deformation mechanics of non-planar topologically interlocked assemblies with structural hierarchy and varying geometry, Sci. Rep. 7 (1) (2017), https://doi.org/10.1038/s41598-017-12147-3.

[24] V. Slesarenko, N. Kazarinov, S. Rudykh, Distinct failure modes in bio-inspired 3D-printed staggered composites under non-aligned loadings, Smart Mater. Struct. 26 (3) (2017) 035053, https://doi.org/10.1088/1361-665X/aa59eb.

[25] M. Mirkhalaf, A. Sunesara, B. Ashrafi, F. Barthelat, Toughness by segmentation: Fabrication, testing and micromechanics of architectured ceramic panels for impact applications, Int. J. Solids Struct. 158 (2019) 52–65.

[26] E.A. Flores-Johnson, L. Shen, I. Guiamatsia, G.D. Nguyen, Numerical investigation of the impact behaviour of bioinspired nacre-like aluminium composite plates, Compos. Sci. Technol. 96 (2014) 13–22.

[27] L.K. Grunenfelder, N. Suksangpanya, C. Salinas, G. Milliron, N. Yaraghi, S. Herrera, K. Evans-Lutterodt, S.R. Nutt, P. Zavattieri, D. Kisailus, Bio-inspired impact-resistant composites, Acta Biomater 10 (9) (2014) 3997–4008.

[28] G.X. Gu, M. Takaffoli, M.J. Buehler, Hierarchically Enhanced Impact Resistance of Bioinspired Composites, Adv. Mater 29 (28) (2017) 1700060, https://doi.org/10.1002/adma.v29.2810.1002/adma.201700060.

[29] S. Khandelwal, T. Siegmund, R.J. Cipra, J.S. Bolton, Transverse loading of cellular topologically interlocked materials, Int. J. Solids Struct. 49 (18) (2012) 2394–2403.

[30] A. Autruffe, F. Pelloux, C. Brugger, P. Duval, Y. Bréchet, M. Fivel, Indentation Behaviour of Interlocked Structures Made of Ice: Influence of the Friction Coefficient, Adv. Eng. Mater. 9 (8) (2007) 664–666.

[31] M. Dugué, M. Fivel, Y. Bréchet, R. Dendievel, Indentation of interlocked assemblies: 3D discrete simulations and experiments, Comput. Mater. Sci. 79 (2013) 591–598.

[32] M. Mirkhalaf, T. Zhou, F. Barthelat, Simultaneous improvements of strength and toughness in topologically interlocked ceramics, Proc. Natl. Acad. Sci. USA 115 (37) (2018) 9128–9133.

[33] A.V. Dyskin, Y. Estrin, E. Pasternak, H.C. Khor, A.J. Kanel-Belov, Fracture resistant structures based on topological interlocking with non-planar contacts, Adv. Eng. Mater. 5 (3) (2003) 116–119.

[34] K. Kourou, T.P. Exarchos, K.P. Exarchos, M.V. Karamouzis, D.I. Fotiadis, Machine learning applications in cancer prognosis and prediction, Comput. Struct. Biotechnol. J. 13 (2015) 8–17.

[35] J. Vamathevan, D. Clark, P. Czodrowski, I. Dunham, E. Ferran, G. Lee, B. Li, A. Madabhushi, P. Shah, M. Spitzer, S. Zhao, Applications of machine learning in drug discovery and development, Nat. Rev. Drug Discov. 18 (6) (2019) 463–477.

[36] B.J. Erickson, P. Korfiatis, Z. Akkus, T.L. Kline, Machine Learning for Medical Imaging(1), Radiographics 37 (2) (2017) 505–515.

[37] G.X. Gu, C.-T. Chen, D.J. Richmond, M.J. Buehler, Bioinspired hierarchical composite design using machine learning: simulation, additive manufacturing, and experiment, Mater. Horiz. 5 (5) (2018) 939–945.

[38] G. Pilania, C. Wang, X. Jiang, S. Rajasekaran, R. Ramprasad, Accelerating materials property predictions using machine learning, Sci. Rep. 3 (1) (2013), https://doi.org/10.1038/srep02810.

[39] C. Bisagni, L. Lanzi, Post-buckling optimisation of composite stiffened panels using neural networks, Compos. Struct. 58 (2) (2002) 237–247.

[40] Z. Zhang, K. Friedrich, Artificial neural networks applied to polymer composites: a review, Compos. Sci. Technol. 63 (14) (2003) 2029–2044.

[41] G.B. Goh, N.O. Hodas, A. Vishnu, Deep learning for computational chemistry, J. Comput. Chem. 38 (16) (2017) 1291–1307.

[42] Y. Liu, T. Zhao, W. Ju, S. Shi, Materials discovery and design using machine learning, J. Materiomics 3 (3) (2017) 159–177.

[43] R. Liu, A. Kumar, Z. Chen, A. Agrawal, V. Sundararaghavan, A. Choudhary, A predictive machine learning approach for microstructure optimization and materials design, Sci Rep 5 (1) (2015), https://doi.org/10.1038/srep11551.

[44] H.T. Kollmann et al., Deep learning for topology optimization of 2D metamaterials, Mater. Des. 196 (2020) 109098.

[45] D.W. Abueidda, S. Koric, N.A. Sobh, Topology optimization of 2D structures with nonlinearities using deep learning, Comput. Struct. 237 (2020) 106283.

[46] Y. Yu, T. Hur, J. Jung, I.G. Jang, Deep learning for determining a near-optimal topological design without any iteration, Struct. Multidiscip. Optim. 59 (3) (2019) 787–799.

[47] D.W. Abueidda et al., Deep learning for plasticity and thermo-viscoplasticity, Int. J. Plast. 136 (2021) 102852.

[48] M. Mozaffar, R. Bostanabad, W. Chen, K. Ehmann, J. Cao, M.A. Bessa, Deep learning predicts path-dependent plasticity, Proc. Natl. Acad. Sci. USA 116 (52) (2019) 26414–26420.

[49] R.G. Budynas, J.K. Nisbett, Shigley's mechanical engineering design, vol. 8, McGraw-Hill, New York, 2008.

[50] R.B. Hetnarski, M.R. Eslami, G. Gladwell, Thermal stresses: advanced theory and applications, vol. 158, Springer, 2009.

[51] C.M. Bishop, Pattern recognition and machine learning, Springer, 2006.

[52] D.W. HOSMER, T. HOSMER, S. LE CESSIE, S. LEMESHOW, A comparison of goodness-of-fit tests for the logistic regression model, Stat Med 16 (9) (1997) 965–980.

[53] Y.Z. Li, Y. Yuan, Convergence Analysis of Two-layer Neural Networks with ReLU Activation, Adv. Neur. Inform. Process. Syst. 30 (Nips 2017) (2017) 597–607.

[54] K. Eckle, J. Schmidt-Hieber, A comparison of deep networks with ReLU activation function and linear spline-type methods, Neural Netw 110 (2019) 232–242.

[55] I. Esmail, H. Yazdani Sarvestani, J. Gholipour, B. Ashrafi, Engineered net shaping of alumina ceramics using picosecond laser, Opt. Laser Technol. 135 (2021) 106669, https://doi.org/10.1016/j.optlastec.2020.106669.

[56] A. Rahimizadeh, H. Yazdani Sarvestani, L. Li, J. Barroeta Robles, D. Backman, L. Lessard, B. Ashrafi, Engineering toughening mechanisms in architected ceramic-based bioinspired materials, Mater. Des. 198 (2021), https://doi.org/10.1016/j.matdes.2020.109375 109375.